Geometric and Electronic Structures of the Ni^{I} and Methyl−Ni^{III} Intermediates of Methyl-Coenzyme M Reductase[†]

Ritimukta Sarangi,*[,‡] Mishtu Dey,[§] and Stephen W. Ragsdale*[,§]

Stanford Synchrotron Radiation Lightsource, SLAC National Accelerator Laboratory, Menlo Park, California 94025, and Department of Biological Chemistry, University of Michigan, Ann Arbor, Michigan 48109-0606

Received January 23, 2009; Revised Manuscript Received February 25, 2009

ABSTRACT: Methyl-coenzyme M reductase (MCR) catalyzes the terminal step in the formation of biological methane from methyl-coenzyme M (Me-SCoM) and coenzyme B (CoBSH). The active site in MCR contains a Ni−F_{430} cofactor, which can exist in different oxidation states. The catalytic mechanism of methane formation has remained elusive despite intense spectroscopic and theoretical investigations. On the basis of spectroscopic and crystallographic data, the first step of the mechanism is proposed to involve a nucleophilic attack of the Ni^{I} active state (MCR_{red1}) on Me-SCoM to form a Ni^{III}−methyl intermediate, while computational studies indicate that the first step involves the attack of Ni^{I} on the sulfur of Me-SCoM, forming a $CH_3^{\bullet}$ radical and a Ni^{II}−thiolate species. In this study, a combination of Ni K-edge X-ray absorption spectroscopic (XAS) studies and density functional theory (DFT) calculations have been performed on the Ni^{I} (MCR_{red1}), Ni^{II} ($MCR_{red1-silent}$), and Ni^{III}−methyl (MCR_{Me}) states of MCR to elucidate the geometric and electronic structures of the different redox states. Ni K-edge EXAFS data are used to reveal a five-coordinate active site with an open upper axial coordination site in MCR_{red1}. Ni K-pre-edge and EXAFS data and time-dependent DFT calculations unambiguously demonstrate the presence of a long Ni−C bond (∼2.04 Å) in the Ni^{III}−methyl state of MCR. The formation and stability of this species support mechanism I, and the Ni−C bond length suggests a homolytic cleavage of the Ni^{III}−methyl bond in the subsequent catalytic step. The XAS data provide insight into the role of the unique F_{430} cofactor in tuning the stability of the different redox states of MCR.

Methyl-coenzyme M reductase (MCR)[1] from methanogenic archaea (*1*) catalyzes the terminal step in biological methane synthesis. Using coenzyme B (CoBSH) as the two-electron donor, MCR reduces methyl-coenzyme M (methyl-SCoM) to form methane and the heterodisulfide product, CoBS−SCoM (*2, 3*). MCR contains an essential redox active nickel tetrapyrrolic cofactor called coenzyme F_{430} at its active site (*4, 5*), which is active in the reduced Ni^{I} state (MCR_{red1}). All of the biologically generated methane, amounting to 1 billion tons per annum globally, is formed by MCR. Furthermore, recent evidence indicates that anaerobic methane oxidation is also catalyzed by MCR and occurs by a reversal of the methane synthesis reaction (*6, 7*). The central role of MCR in the synthesis of this important fuel, which is also a potent greenhouse gas, makes it important to understand the catalytic mechanism of methane formation.

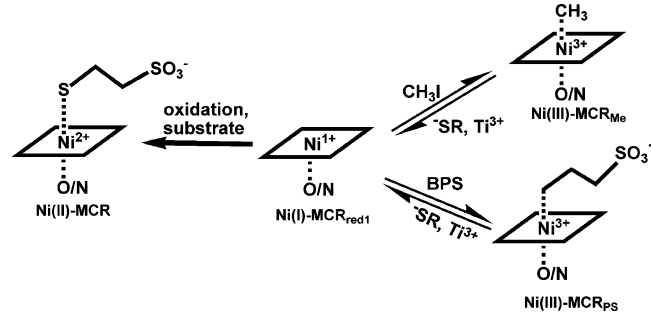

FIGURE 1: Schematic diagram showing the proposed structures upon conversion of the active MCR_{red1} to $MCR_{red1-silent}$ and MCR_{Me}. The Ni^{III}−PS state is analogous to the Ni^{III}−methyl state and is formed by the reaction of MCR_{red1} with bromopropane sulfonate.

Two limiting mechanisms for MCR-catalyzed methane formation have been proposed (Figure 1). In mechanism I, based on the Ni^{II} crystal structure and model chemistry (*8*−*11*), Ni^{I} performs an S_N2 attack on the methyl group of methyl-SCoM to form a Ni^{III}−methyl intermediate that undergoes one-electron reduction to form a Ni^{II}−methyl species, which then undergoes protonation to form methane, and a $CoMS^{\bullet}$ radical. Condensation of the $CoMS^{\bullet}$ radical with CoBSH generates a $CoBSSCoM^{\bullet}$ radical anion that reduces Ni^{II} to the active Ni^{I} state. Mechanism II, which is based on density functional theory calculations (*12, 13*) and considers Ni^{III} not to be a feasible intermediate, proposes that Ni^{I}−MCR_{red1}

[†] This work has been supported by NIH Grant 1P20RR17675 to S.W.R. We are grateful for funding from a Department of Energy grant (DE-FG02-08ER15931) to S.W.R.

* To whom correspondence should be addressed. R.S.: e-mail, ritis@slac.stanford.edu; phone, (650) 926-4621; fax, (650) 926-4100. S.W.R.: e-mail, sragsdal@umich.edu; phone, (734) 615-4621; fax, (734)763-4581.

[‡] SLAC National Accelerator Laboratory.

[§] University of Michigan.

[1] Abbreviations: CoBSH, coenzyme B; DFT, density functional theory; ENDOR, electron nuclear double resonance; EPR, electron paramagnetic resonance; EXAFS, extended X-ray absorption fine structure; MCR, methyl-coenzyme M reductase; methyl-SCoM, methyl-coenzyme M; PDB, Protein Data Bank; TD-DFT, time-dependent density functional theory; XAS, X-ray absorption spectroscopy.

10.1021/bi900087w CCC: $40.75
Published on Web 02/25/2009

reacts with the sulfur of Me-SCoM to generate a methyl radical and a Ni^{II}−thiolate complex. The methyl radical is proposed to abstract a hydrogen atom from CoBSH to generate a CoBS$^{\bullet}$ radical that reacts with bound CoM to generate Ni^{II} and the same CoBS−SCoM$^{\bullet}$ radical anion proposed in mechanism 1. Finally, reduction of Ni^{II} and generation of the CoBS−SCoM product occur as in mechanism I. The major distinction between the two mechanisms lies in the intermediate generated in the first step of catalysis: Ni^{III}−methyl or methyl radical and Ni^{II}−SCoM. However, so far, none of the proposed intermediates have been trapped during reactions with the natural substrates; presumably, these intermediates form and decay too fast to be observed by stopped-flow and rapid freeze quench EPR methods.

Much of our understanding of the structure and mechanism of MCR catalysis is based on crystal structures of various inactive Ni^{II} states (MCR_{silent}, $MCR_{ox1-silent}$, and $MCR_{red1-silent}$) (*8, 10, 14*), since the crystal structures of the active states of MCR have not been reported. In all states, the central Ni atom is coordinated by four corphin ring nitrogens and a lower axial glutamine oxygen atom. The upper axial ligands in $MCR_{ox1-silent}$ and MCR_{silent} are the thiol group of coenzyme M and the sulfonate oxygen of the heterodisulfide product, respectively (*8, 10, 14*). In $MCR_{red1-silent}$, two structures have been proposed: a five-coordinate site lacking an upper axial ligand and a six-coordinate site with the thiol group of coenzyme M as the upper axial ligand (*10*). EXAFS studies have also been performed on various Ni^{II} forms of MCR, which are consistent with crystal structures; however, high-*k* EXAFS studies have not been reported (*8, 15*).

In this study, Ni^{I} and Ni^{III}−methyl species, which are the starting state and a putative intermediate state in the MCR-catalyzed reaction, respectively, have been trapped and characterized. Although a Ni^{III}−methyl intermediate has not yet been identified during the reaction with the natural substrate Me-SCoM, its formation has been demonstrated in the reaction of MCR_{red1} with methyl bromide (*16*) and methyl iodide (*17*). Analogous Ni^{III}−alkyl species are formed by the reaction of MCR_{red1} with corresponding alkyl halides (*18*−*20*). Furthermore, this species has been shown to react with HSCoM (and other thiolates) to generate the Ni^{I}−MCR_{red1} state and methyl-SCoM (or other alkyl thioethers). The similarity between the rate constants for methane formation from the MCR_{Me} species with HSCoM and CoBSH (1.1 s^{-1}) and the steady-state k_{cat} for methane formation from natural substrates (4.5 s^{-1} at 25 °C) is consistent with the catalytic intermediacy of the methyl−Ni species (*17*). Thus, there is significant evidence supporting the catalytic relevance of the MCR_{Me} intermediate. Although the crystal structure of active MCR_{red1} is not known, much of our understanding about the active site structure in MCR_{red1} comes from Ni K-edge EXAFS studies. Two structures have been proposed: a five-coordinate site with an open upper axial ligand (*8*) and a six-coordinate site with an oxygen atom as the upper axial ligand (*15*). However, in both studies, the *k* range for the reported EXAFS data was 2−12 $Å^{-1}$, limiting the resolution (±0.16 Å) and the ability to identify and distinguish the equatorial and axial ligands.

The goal of this study was to determine high-resolution structures of the active Ni^{I} state with accurate metrical parameters. Although direct structural information about the Ni^{III}−methyl state is not available, EPR, ENDOR, and HYSCORE spectroscopic studies have determined the electronic structure of the active site Ni center (*16, 17*). These studies describe MCR_{Me} to be formally Ni^{III} with a methyl−Ni bond formed by the oxidative addition reaction of methyl iodide with the Ni^{I}−MCR_{red1} complex. The presence of a large ^{13}C hyperfine coupling indicates that the methyl group is coordinated to the paramagentic Ni^{III} center by a covalent bond, with a Ni−C bond distance of approximately 1.9−2.0 Å (*16, 17*), although the actual bond distance cannot be precisely determined by analysis of these hyperfine couplings. Similarly, EPR studies on the adduct between propanesulfonate and MCR demonstrated the presence of a Ni(III)−C bond with an approximate bond distance of 2 Å (*21*). However, the active site geometry of the MCR_{Me} state has not been determined by any structure determination technique.

In the work described here, Ni K-pre-edge and edge X-ray absorption spectroscopy and EXAFS investigations have been combined with time-dependent density functional theory (DFT) calculations to determine the local geometric structure at the active sites in $MCR_{red1-silent}$, MCR_{red1}, and MCR_{Me}. The ∼0.1 Å resolution ($k = 17$ $Å^{-1}$) EXAFS data presented here provide a precise description of the active site geometry in the active MCR_{red1} state with the ability to differentiate between the axial Ni−O(Gln) bond distance and the Ni−N(F_{430}) distances. This ability to discriminate the axial and equatorial bond distances was not present in previously reported EXAFS data, which extended up to $k = 12$ $Å^{-1}$ (*8, 15*). The results presented in this study also provide the first experimentally determined atomic-level description of the Ni center in the proposed intermediate methyl−Ni state with precise Ni−first neighbor bond distance measurements. The trends in the Ni K-pre-edge and edge energy positions are used to determine the changes in bonding and ligand field. Together, the XAS and EXAFS studies are used to provide insight into the electronic structures of the active sites and how they relate to the mechanism of formation of methane by MCR.

EXPERIMENTAL PROCEDURES

Sample Preparation. (i) Material and Organisms. Methanothermobacter marburgensis was obtained from the Oregon Collection of Methanogens catalogue as OCM82. All buffers, mediUM ingredients, and other reagents were acquired from Sigma-Aldrich and, unless otherwise stated, were of the highest purity available. Solutions were prepared using nanopure deionized water. N_2 (99.98%), H_2/CO_2 (80%/20%), and ultra-high-purity (UHP) H_2 (99.999%) were obtained from Cryogenic Gases (Grand Rapids, MI). Ti(III) citrate solutions were prepared from a stock solution of 200 mM Ti(III) citrate, which was synthesized by adding sodium citrate to Ti(III) trichloride (30 wt % solution in 2 N hydrochloric acid) under anaerobic conditions and adjusting the pH to 7.0 with sodium bicarbonate. The concentration of Ti(III) citrate was determined routinely by titrating against a methyl viologen solution.

(ii) M. marburgensis Growth, Harvest, and MCR_{red1} Purification. MCR_{red1} was isolated from *M. marburgensis* cultured on H_2/CO_2 (80%/20%) at 65 °C in a 14 L fermentor. Culture media were prepared as previously described (*18*) with a slight modification of the sulfur and reducing source. Instead of H_2S used previously, 50 mM sodium sulfide was

added at a flow rate of 1 mL/min during the entire growth period. MCR_{red1} was generated in vivo and purified as described previously (*18*). This purification procedure routinely generates ~70% MCR_{red1} as determined by UV−visible and EPR spectroscopy.

(iii) Preparation of MCR_{red1} and MCR_{Me} Samples. MCR_{red1} was prepared in 50 mM Tris-HCl (pH 7.6) containing 30% glycerol. The MCR_{Me} samples were prepared in the anaerobic chamber by incubating MCR_{red1} with excess methyl iodide in 50 mM Tris-HCl (pH 7.6). The reaction mixture was split into three aliquots. One sample was transferred to a cuvette to monitor the conversion of the $Ni^{I}-MCR_{red1}$ complex to Ni^{III}/Ni^{II} by UV−visible spectroscopy; a second aliquot was frozen in liquid nitrogen in an EPR tube to measure the concentration of MCR_{Me} species, and a third sample was loaded in 1 mm lucite cells with 37 μm Kapton windows for X-ray absorption studies, frozen in liquid nitrogen, and maintained under liquid N_2 conditions until data were collected. An important point to note is that the reaction of MCR_{red1} to MCR_{Me} always goes to at least 100% conversion, if not more. This observation has been made repeatedly, and in these studies, we observed a 3% increase in the MCR_{Me} concentration compared to the starting MCR_{red1} concentration that was used.

X-ray Absorption Spectroscopy. Ni K-edge X-ray absorption spectra of $MCR_{red1-silent}$, MCR_{red1}, and MCR_{Me} were measured at the Stanford Synchrotron Radiation Laboratory on 16-pole, 2.0 T, wiggler beamline 9-3. A liquid N_2-cooled Si(220) double-crystal monochromator was used for energy selection. A Rh-coated harmonic rejection mirror and a cylindrical Rh-coated bent focusing mirror were used. An Oxford Instruments CF1208 continuous-flow liquid He cryostat was used to maintain the sample temperature at ~10 K throughout the course of data measurement. Data were measured up to $k = 18$ Å^{-1} in fluorescence mode using a Canberra Ge-30 element array detector. Internal energy calibration was accomplished by simultaneous measurement of the absorption of a Ni foil placed between two ionization chambers situated downstream of the sample. The first inflection point of the Ni foil was assigned to 8331.6 eV. All samples were closely monitored for photoreduction. However, the Ni active site in all three states of the protein was resistant to photoreduction. Spectra presented here are a 10-scan, 24-scan, and 28-scan average for $MCR_{red1-silent}$, MCR_{red1}, and MCR_{Me}, respectively. The energy-calibrated data were averaged and processed by fitting a second-order polynomial to the pre-edge region, which was subtracted from the entire spectrum as background using Pyspline (*22*). A three-region spline function of order 2,3 and 3 was used to model the background atomic absorption and subtracted from the spectrum. Normalization was accomplished by dividing the entire spectrum by a polynomial of order 1, which was fit to the postedge region. The experimental threshold energy was chosen to be 8340 eV (*8, 15*). The intensities and energies of the pre-edge transitions were quantitated by performing least-squares refinement using EDG−FIT (*23*). The pre-edge features were modeled by using 1:1 Gaussian/Lorentzian Pseudo-Voigt line shapes to simulate the convolution of instrument and core-hole lifetime broadening. Additional Pseudo-Voigt line shapes were also required to mimic the rising-edge transition and shoulders in the edge region. The data were fit over two different energy ranges: 8125−8135 and 8127−8140 eV. The least-squares error and a comparison of the second derivatives of the data and fit were used to estimate the goodness of the fit. Standard deviations in energy position and intensity were used to quantitate the errors in these parameters. Theoretical EXAFS phase and amplitude parameters were calculated using FEFF (Macintosh version 8.4) (*24−26*) and the published crystal structure of $MCR_{red1-silent}$ (PDB entry 1MRO) (*27*) as the initial starting model. Data were fit using EXAFSPAK (*23*). The metrical parameters obtained by fitting the data indicated significant differences in the local structures of MCR_{red1}, $MCR_{red1-silent}$, and MCR_{Me} around the central absorbing Ni atom. On the basis of these preliminary fits, a new set of theoretical EXAFS signals, $\chi(k)$, were calculated, and the data for MCR_{red1} and MCR_{Me} were refit using the new theoretical parameters generated from their individual refined models. The structural parameters varied during the fitting process were restricted to the bond distance (R) and the bond variance (σ^2), which is related to the Debye−Waller factor, resulting from a combination of static and dynamic disorder (due to thermal motion) between the absorber and scatterer pair. The nonstructural parameter, ΔE_0, was also allowed to vary but was restricted to a common value for every component in a given fit. Coordination numbers were systematically varied in the course of a fit but were fixed within a given fit. In the case of MCR_{red1} and MCR_{Me}, which were estimated to have 36 and 33% of the $MCR_{red1-silent}$ decay product using UV−vis spectroscopy, respectively, partial coordination numbers were also explored during the course of the fit. It should be noted that the EXAFS fits to the data were performed between $k = 2$ and 17 Å^{-1}. Since, the Fourier transform intensity, R', is significant between 1.5 and 4 Å, the number of independent parameters is 26 (using the formula $2\delta k\delta R'/\pi + 2$) (*28*). The maximum number of independent parameters used in the fits is 13, which is lower than the number of maximum allowed independent parameters.

DFT Calculations. Gradient-corrected (GGA), spin-unrestricted density functional theory calculations were performed using the Gaussian03 (*29*) package on a 32-CPU Linux cluster. Geometry optimizations were performed in each case. The B3LYP (*30−32*) hybrid functional and the following basis sets were employed: triple-ζ 6-311+G* (*33−35*) on Ni, 6-311G* (*33−35*) on S, and 6-31G* (*36−38*) on O, C, H, and N. The input structures were based on the published crystal structure and the EXAFS best-fit results presented herein. The transaxial glutamine ligand was fixed at the EXAFS distance for MCR_{red1} DFT calculations. Time-dependent DFT calculations were performed with the electronic structure program ORCA (*39, 40*) to calculate the energies and intensities of the Ni 1s → 3d pre-edge transitions. Single-point ground-state calculations were performed using the geometry-optimized coordinates obtained from the Gaussian03 package. The BP86 functional and the following basis sets were employed: CP(PPP) (*41, 42*) on Ni (core properties basis set as implemented in ORCA) and TZVP (*43, 44*) on N, C, H, O, and S. Tight convergence criteria was imposed on all calculations. The calculated energies and intensities were convoluted with a Gaussian function with half-widths of 1.4 eV (*45*) to account for core-hole and instrument broadening. Calculations were performed in a dielectric continuum using the conductor-like screening

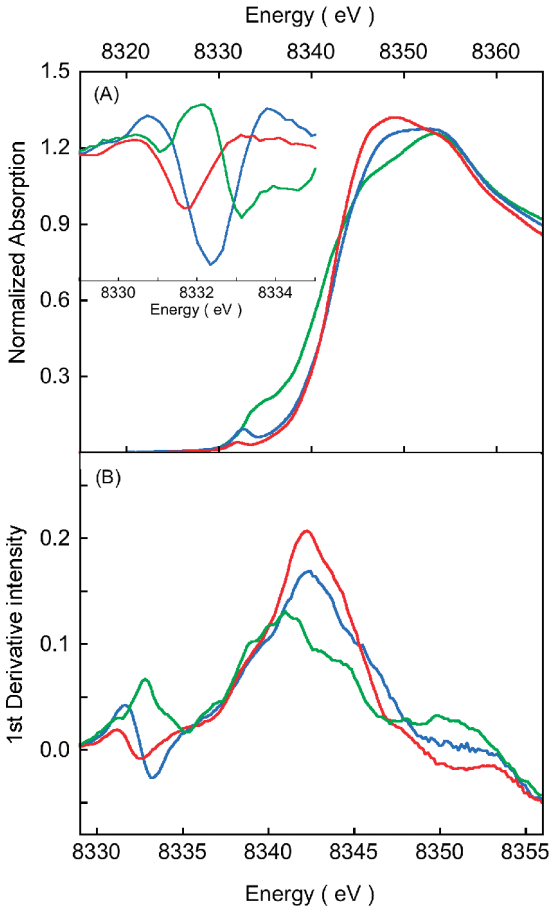

FIGURE 2: (A) Normalized Ni K-edge XAS spectra of $MCR_{red1-silent}$ (red), MCR_{red1} (green), and MCR_{Me} (blue). The inset shows the expanded second-derivative spectrum. (B) First-derivative spectrum showing the edge inflection points.

model (COSMO). A shift of 223.0 eV was applied to the calculated pre-edge energy positions. This is usually the case with core-level TD-DFT calculation since DFT does not calculate core potentials accurately, resulting in the core levels being too high relative to the valence levels.

RESULTS

Ni K-Edge XAS. The normalized Ni K-edge XAS spectra of MCR_{red1}, $MCR_{red1-silent}$, and MCR_{Me} are shown in Figure 2 (*46*). The inset shows the expanded spectra of the second derivative of the pre-edge region. The $MCR_{red1-silent}$ data presented here agree well with the previously published XAS data of Duin et al. (*8*). The pre-edge feature observed at ~8332 eV occurs due to an electronic dipole-forbidden quadrupole-allowed transition from the Ni 1s orbital to valence orbitals with significant Ni 3d character (*47, 48*). This formally forbidden transition gains intensity from Ni 3d-4p mixing due to deviation of the absorbing Ni center from centrosymmetry (*49*). The pre-edge energy position dominantly reflects the change in the ligand field strength (LF) felt by the absorbing Ni atom and shifts to a higher energy with an increase in LF (*50, 51*). Least-squares fits reveal that the pre-edge transitions for MCR_{red1}, $MCR_{red1-silent}$, and MCR_{Me} occur at 8331.5, 8332.0, and 8332.6 eV, respectively (Table 1), indicating an increase in ligand field on going from MCR_{red1} to $MCR_{red1-silent}$ to MCR_{Me}. In addition to the shift in the pre-edge energy position, an increase in the pre-edge intensity is observed for MCR_{Me} relative to MCR_{red1} and $MCR_{red1-silent}$ (Table 1), indicating a significant increase in the level of 4p mixing in MCR_{Me}. A comparison of the Ni K-rising-edge spectra of MCR_{red1}, $MCR_{red1-silent}$, and MCR_{Me} is shown in Figure 2. The rising-edge energy positions (approximated to the first inflection points) for MCR_{red1}, $MCR_{red1-silent}$, and MCR_{Me} occur at 8341.0, 8342.2, and 8342.4 eV, respectively.

Table 1: Ni K-Pre-Edge and Edge Energy Positions and Intensities

protein	pre-edge energy (eV)[a,b]	pre-edge intensity ($\times 10^{-2}$)[b]	edge inflection (eV)
MCR_{red1}	8331.5 ± 0.04	5.3 ± 1.8[c]	8341.0
$MCR_{red1-silent}$	8332.0 ± 0.02	5.1	8342.2
MCR_{Me}	8332.6 ± 0.02	15.7	8342.4

[a] The spectral broadening is ~1.4 eV. [b] The errors in pre-edge energy position obtained from a statistical analysis over several best fits are given. The systematic error due to monochromator energy drift and calibration is less than 0.04 eV. [c] The error in total intensity estimation due to data processing and statistical estimation of the standard deviation is $\pm 0.5 \times 10^{-2}$. The error in intensity estimation of MCR_{red1} is higher due to the presence of low-lying edge transitions.

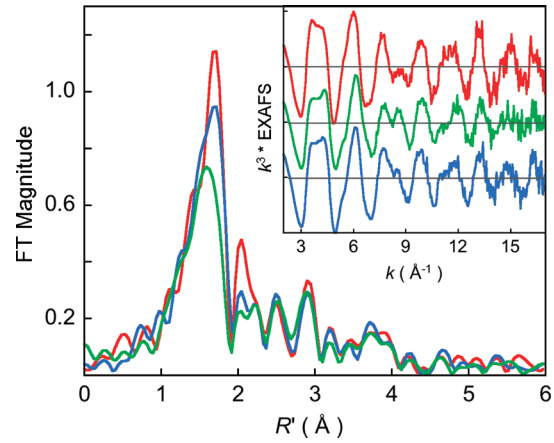

FIGURE 3: Comparison of the k^3-weighted Ni K-edge EXAFS for $MCR_{red1-silent}$ (red), MCR_{red1} (green), and MCR_{Me} (blue) and their corresponding Fourier transforms.

EXAFS. A comparison of the k^3-weighted Ni K-edge EXAFS data and their corresponding non-phase shift corrected Fourier transforms (FT) of MCR_{red1}, $MCR_{red1-silent}$, and MCR_{Me} are shown in Figure 3. The EXAFS data for the $MCR_{red1-silent}$ state have been previously reported; however, here, higher-resolution data to $k \sim 17$ Å have been obtained. The resolution in R space is 0.1 Å for all the data sets presented here (*52*). The Fourier transforms indicate that with the transition from $MCR_{red1-silent}$ to MCR_{red1} there is a sharp decrease in the first-shell intensity at ~1.5 Å, in addition to a small shift to a lower R' (angstroms) (*53*). With the transition from MCR_{red1} to MCR_{Me}, the first-shell peak shifts to a higher R' and gains intensity. Beyond the first shell, the $MCR_{red1-silent}$ Fourier transform has significant intensity at $R' \sim 2.0$ Å, which is absent in both MCR_{red1} and MCR_{Me} forms. The Fourier transform intensities resulting from the second- and third-shell single and multiple scattering contributions are very similar in all three forms. Importantly, the MCR_{red1} and MCR_{Me} EXAFS data differ significantly from each other and from the $MCR_{red1-silent}$ data, indicating that the Ni active sites are different in each state.

The k^3-weighted Ni K-edge EXAFS data for $MCR_{red1-silent}$, MCR_{red1}, and MCR_{Me}, their corresponding non-phase shift

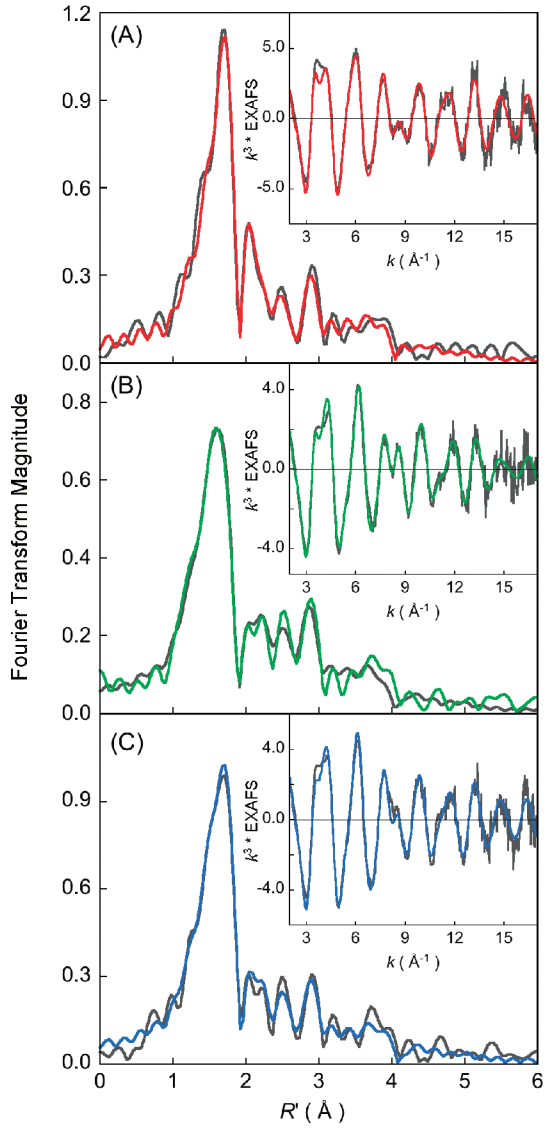

FIGURE 4: k^3-weighted Ni K-edge EXAFS data (inset) and their corresponding Fourier transforms (FT) for (A) $MCR_{red1-silent}$ [data (gray) and fit (red)], MCR_{red1} [data (gray) and fit (green)], and MCR_{Me} [data (gray) and fit (blue)].

corrected Fourier transforms (FTs), and the corresponding fits are presented in panels A−C of Figure 4. The EXAFS best-fit parameters are listed in Table 2. In all fits, the addition of a shell was justified on the basis of a significant decrease in the error function. A complete shell-by-shell analysis is presented in the Supporting Information. The first shell of the EXAFS data for $MCR_{red1-silent}$ was fit with four Ni−N components at 2.09 Å, one Ni−S component at 2.41 Å, and one Ni−O component at 2.26 Å. The second and third shells (2.0−4.5 Å region in the FT spectra) were fit with single-scattering (SS) and multiple-scattering (MS) components from the corphin ring (see Table 2). The SS from the third shell of the corphin ring contributes between ~3.8 and 4.2 Å. Long-range (high-R) SS contributions from light atoms are usually weak and do not significantly contribute to the EXAFS signal. Inclusion of the SS paths (for all three data sets) resulted in negative σ^2 values and did not improve the goodness of fit parameter. However, MS components, which can have significant long-range contributions as a result of the forward focusing effects, could be included and resulted in a statistically significant decrease in the goodness of fit parameter (see the shell-by-shell fit in the Supporting Information). The first shell of the EXAFS data for MCR_{red1} was fit with four Ni−N components at 2.05 Å and a weak Ni−O component at 2.25 Å. The best fit to the data furnishes a high σ^2 value for the first-shell Ni−N component at 2.05 Å, indicating a high level of disorder in the Ni−N(corphin) bond distances. The second and third shells were fit with single-scattering (SS) and multiple-scattering (MS) components from the corphin ring (Table 2). Since the MCR_{red1} sample was contaminated with ~36% of the $MCR_{red1-silent}$ decay form, a 0.36 Ni−S component was included and proved to be necessary for obtaining a good fit. In the case of MCR_{Me}, the first shell of the EXAFS data was fit with five Ni−N components at 2.08 Å and a weak Ni−O component at 2.32 Å. Split first-shell fits were also performed which resulted in a best fit with one Ni−C component at 2.0 Å, four Ni−N components at 2.08 Å, and a very weak Ni−O component at 2.32 Å. However, the error value did not improve significantly to justify the addition of two independent parameters resulting from the split first shell. The second and third shells were fit with single-scattering (SS) and multiple-scattering (MS) components from the corphin ring. Since the MCR_{Me} sample was contaminated with ~33% of the $MCR_{red1-silent}$ decay form, a 0.33 Ni−S component was included and proved to be necessary for obtaining a good fit. For all three data sets, the second and third shell were fit using the same number and type of SS and MS components.

ANALYSIS

Ni K-Pre-Edge TD-DFT Calculations. The geometric and electronic structure of $MCR_{red1-silent}$ has been well characterized using X-ray diffraction and optical spectroscopic techniques, which indicate a six-coordinate high-spin $S = 1$ d^8 Ni^{II} species with a d_{z^2} ground state (*27, 55, 56*). Thus, it is expected that two 1s → 3d transitions corresponding to the two singly occupied d_{z^2} and $d_{x^2-y^2}$ orbitals should be present. However, the spectral broadening at the Ni K-edge is ~1.4 eV which does not allow the two pre-edge features to be well-resolved. In addition, the overlap of the pre-edge with the intense rising-edge transition renders it impossible to separate out the two 1s → 3d transitions. Thus, the average energy of the two 1s → 3d transitions is determined to be 8332.0 eV.

The one-electron reduced MCR_{red1} form is an $S = {}^1/_2$ d^9 species with a $d_{x^2-y^2}$ ground state, indicating that the d_{z^2} hole becomes occupied upon reduction and loss of the upper axial ligand (*1, 57, 58*). The pre-edge energy position in MCR_{red1} is shifted to lower energy (by 0.6 eV) compared to $MCR_{red1-silent}$. This is consistent with a decrease in LF associated with the decrease in the number of ligands from six ($MCR_{red1-silent}$) to five (MCR_{red1}) (see Table 2). It is important to note here that although the ligand field in MCR_{red1} has decreased relative to that in $MCR_{red1-silent}$, the energy position (8331.5 eV) is comparable to those of other covalent Ni^{II} compounds (*59, 60*), indicating a strong ligand field at the Ni active site exerted due to the presence of the equatorial F_{430} cofactor. In $MCR_{red1-silent}$, the axial bond distances are longer by ~0.04 Å, which might suggest that the pre-edge energy position of $MCR_{red1-silent}$ should be lower than in MCR_{red1}. However, the presence of a strong Ni−S

Table 2: Ni K-Edge EXAFS Least-Squares Fitting Results[a]

	$MCR_{red1-silent}$					MCR_{red1}					MCR_{Me}				
path	no.	R (Å)[b]	σ^2 (Å^2)[c]	ΔE_0 (eV)	F[d]	no.	R (Å)[b]	σ^2 (Å^2)[c]	ΔE_0 (eV)	F[d]	no.	R (Å)[b]	σ^2 (Å^2)[c]	ΔE_0 (eV)	F[d]
Ni−N	4	2.09	298			4	2.05	624			5	2.08	591		
Ni−O	1	2.26	382			1	2.25	949			1	2.32	951		
Ni−S	1	2.41	644	13.08	0.37	0.36	2.41[e]	87	12.93	0.19	0.33	2.41[e]	81	13.58	0.27
Ni−C	6	3.01	720			6	3.02	604			6	3.03	641		
Ni−C/N	12	3.20	288			12	3.21	415			12	3.23	291		
Ni−C/N	12	4.43	924			12	4.41	801			12	4.38	588		

[a] The S_0^2 value was fixed at 1 for all refinements. The positive ΔE_0 value is justified on the basis of the choice of threshold energy (*54*). [b] Estimated standard deviations in the distances are ±0.02 Å. [c] The σ^2 values have been multiplied by 10^5. [d] The error is given by $[(\chi_{obsd} - \chi_{calcd})^2 k^6]/[(\chi_{obsd}^2) k^6]$. [e] The distance for the Ni−S path was kept fixed in the case of MCR_{red1} and MCR_{Me}.

Table 3: Selected DFT Parameters

	bond distance (Å)[b]				Löewdin charge		Mulliken population (%)	
model	$Ni-N_{1(2)}$	$Ni-N_{3(4)}$	Ni−O	Ni−S/C	Ni	F_{430}[c]	$Ni(3d_{z^2}+3d_{x^2-y^2})$[d]	$Ni(3d_{xz}+3d_{yz})$[e]
MCR_{red1}[a]	1.99 (1.99)	2.15 (2.06)	2.25	−	0.21	−0.30	54	72
$MCR_{red1-silent}$	2.06 (2.06)	2.12 (2.12)	2.26	2.44	0.22	−0.12	141	−
MCR_{Me}	2.04(2.02)	2.20 (2.10)	2.32	2.00	0.32	0.26	150	−

[a] The calculations were performed on simplified models (shown in Figure 6). [b] The numbering of the Ni−N bonds is explained in Figure S2 of the Supporting Information. [c] The charge on the entire corphin ring. [d] The combined contribution of the antibonding Ni $3d_{x^2-y^2}$ and $3d_{z^2}$ to the valence orbitals. In the case of MCR_{red1}, only $3d_{x^2-y^2}$ character is present. [e] Valence Ni $3d_{yz}$ and $3d_{xz}$ character due to back-bonding with filled π^*-type F_{430} orbitals.

ligand in $MCR_{red1-silent}$ compensates for the increase in ligand field in MCR_{red1} due to shortening of the equatorial Ni−N bonds (see Table 1). This increases the ligand field felt at the Ni center in $MCR_{red1-silent}$ and shifts the pre-edge to a higher energy than in MCR_{red1}. The rising-edge spectrum of MCR_{red1} shows two transitions at 8333.5 and 8334.9 eV. These transitions are usually most intense in four-coordinate square planar complexes in ideal D_{4h} geometry and lose intensity as the site symmetry deviates from D_{4h} (*61, 62*). These intense edge features can result from the following effects: long-range multiple-scattering effects that are enhanced at the rising edge due to the larger photoelectron mean free path (*63*) and a formally forbidden two-electron shakedown process which becomes allowed in the excited state (*64, 65*). While the shakedown transition is enhanced for compounds that have strong charge transfer transitions or are very covalent (*50, 66*), both effects are enhanced in the D_{4h} symmetry, in which the central atom lies in the plane of the equatorial ligands. The presence of the low-lying edge transition only in the MCR_{red1} form indicates that the Ni^{I} center is closer to the corphin plane relative to the $MCR_{red1-silent}$ or MCR_{Me} forms.

MCR_{Me} has been shown to be a d^7 species with an $S = {}^1/_2$ ground state (*17, 58*). This electronic structure allows for a total of three Ni 1s → 3d transitions contributing to the Ni K-pre-edge transition. It has been previously shown on the basis of EPR data that the ground state is $d_{x^2-y^2}$; thus, the three 1s → 3d transitions are to the β $d_{x^2-y^2}$ and α and β d_{z^2} orbitals. The pre-edge feature for MCR_{Me} has shifted by 1.1 eV to a higher energy compared to that of MCR_{red1}, and the intensity has approximately quadrupled. This indicates a dramatic increase in ligand field and Ni 3d-4p mixing. The pre-edge energy position is higher than that for several other Ni^{III} complexes (pre-edge energy position of ≤8332 eV) supporting the increase in ligand field (*59, 60*). In addition, the EXAFS results indicate that the first-shell coordination has increased from four to five on going from MCR_{red1} to MCR_{Me} (see Results). Together, the pre-edge and EXAFS data indicate that MCR_{Me} has an additional strongly coordinating axial light-atom ligand, consistent with previous EPR/ENDOR (*16, 58*) studies that show the axial ligand to be a methyl group. The presence of a Ni−C axial interaction is also expected to result in a dramatic increase in the Ni $3d_{z^2}$-$4p_z$ mixing and hence the 1s → d_{z^2} (α and β) transition intensity; the pre-edge data directly indicate the presence of a methyl group as the upper axial ligand in MCR_{Me}. Interestingly, although the pre-edge energy position shifts to a higher energy with the transition from $MCR_{red1-silent}$ to MCR_{Me}, the edge inflection points are very similar for the two species (Table 1). This shows that the Q_{Ni} in MCR_{Me} is similar to that in $MCR_{red1-silent}$ (*67*), indicating that the additional hole in MCR_{Me} is spread over the entire corphin ring and the site is best described as $[Ni(F_{430})Me]^+$, where F_{430} represents the corphin ring and the positive charge is delocalized (see Discussion for further analysis of the charge distribution).

To support the Ni K-pre-edge analysis, TD-DFT calculations were performed on starting active site structures of $MCR_{red1-silent}$, MCR_{red1}, and MCR_{Me}, which were generated by considering the crystal structure of $MCR_{red1-silent}$ and the EXAFS data presented herein. Selected DFT parameters are listed in Table 3. The calculated spectra on the geometry-optimized structures are presented in Figure 5. The calculated pre-edge energies are 8118.8, 8119.2, and 8119.6 eV for MCR_{red1}, $MCR_{red1-silent}$, and MCR_{Me}. The trend in energy position is in reasonable agreement with the experimental data (see Table 1).

Fits to the EXAFS data for MCR_{Me} indicate the presence of a weak Ni−O component at 2.32 Å. Since the contribution of a relatively long first-shell light atom to the EXAFS data is usually weak, the fits cannot be definitive indicators of the presence of the long Ni−O component. Hence, to test for the presence of this long Ni−O(Gln) axial interaction, TD-DFT calculations were also performed on a MCR_{Me} model with no axial glutamine ligand (MCR_{Me-NA}). The calculations show that both the relative pre-edge energy and intensity are in worse agreement with the data for the MCR_{Me-NA} model relative to the MCR_{Me} model, strongly

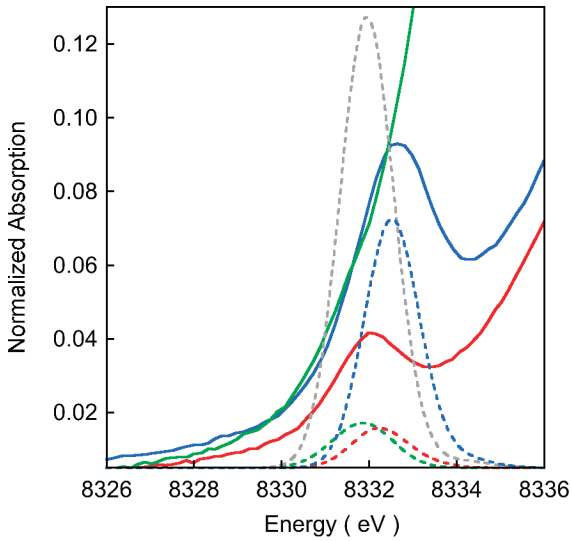

FIGURE 5: (A) Comparison of the Ni K-pre-edge XAS data (—) with the TD-DFT calculated spectra (---): $MCR_{red1-silent}$ (red), MCR_{red1} (green), MCR_{Me} (blue), and MCR_{Me-NA} (gray).

indicating the presence of an axial Ni−O(Gln) bond in MCR_{Me} (Figure 5).

Geometric Structures of MCR_{red1} and MCR_{Me}. The Ni K-edge EXAFS results indicate that the active site in $MCR_{red1-silent}$ is six-coordinate with four Ni−N interactions at 2.08 Å, one Ni−S interaction at 2.41 Å, and one weak Ni−O interaction at 2.27 Å. This is in reasonable agreement with the published crystal structure (PDB entry 1HBO with a resolution of 1.78 Å) (*10, 68*). The crystal structure reveals that $MCR_{red1-silent}$ is a dimer of two $\alpha\beta\gamma$ trimers with nearly identical Ni−porphinoid active sites. The crystal structure also indicates that the Ni cofactor exhibits a large spread in the equatorial Ni−N bond distances, ranging from 1.94 to 2.31 Å. However, fits to the EXAFS data presented here show that the first-shell σ^2 value is low, indicating an ordered first shell, which in turn suggests that in solution the equatorial bond distances of the Ni−porphinoid ring of $MCR_{red1-silent}$ are more symmetric than in the crystal.

The fit to the Ni K-edge EXAFS data of MCR_{red1} indicates a disordered first shell with four Ni−N contributions and a weak axial Ni−O interaction at 2.26 Å. This axial interaction is longer than that reported in a previous EXAFS analysis (2.12 Å); however, the EXAFS data presented in the reported study were limited (k = 2−12 $Å^{-1}$) (*8*), and an accurate estimate of a weak axial ligand was not possible. Our study reveals that with the transition from $MCR_{red1-silent}$ to MCR_{red1}, the axial −SR group is lost and the site becomes disordered. One interesting aspect of the EXAFS data is that the average Ni−N bond distance decreases from 2.09 to 2.05 Å with the transition from $MCR_{red1-silent}$ to MCR_{red1} (*69*). A similar shortening of the bond distance was observed in the EXAFS data for the isolated $Ni^{I}/Ni^{II}F_{430}$ cofactor (*70, 71*). This is counterintuitive since the larger Ni^{I} in MCR_{red1} should lead to longer Ni−N bond distances. However, this shortening of the bond can be explained on the basis of back-bonding from the Ni^{I} center to the low-lying π^* orbitals on the corphin ring (*72*). The charge transfer arising due to back-bonding would be consistent with the low-lying charge transfer transitions observed in the MCD spectrum of MCR_{red1} and low-energy transitions in the Ni K-rising-edge region (*73*). This is also consistent with the valence Mulliken populations obtained from the DFT calculations, which show significant valence Ni $3d_{xz}$ and $3d_{yz}$ character in the valence low-lying orbitals for MCR_{red1} (see Table 3). Thus, a combination of the edge data, the pre-edge energy position, and the EXAFS data reveals a five-coordinate, disordered active site with a weak axial Ni−O bond in MCR_{red1} (Figure 6).

The Ni K-edge EXAFS data for MCR_{Me} are significantly different from those of $MCR_{red1-silent}$ and MCR_{red1}. In particular, the Ni−S contribution seen in $MCR_{red1-silent}$ is not present and the first shell is composed of five light atom ligands [simulated using five Ni−N components (see Table 2)], in contrast to four in MCR_{red1} and $MCR_{red1-silent}$. On the basis of the Ni K-pre-edge data and the TD-DFT calculations, the additional light atom ligand is best described as a methyl group. Since the MCR_{Me} sample had ∼33% $MCR_{red1-silent}$ contamination, fits with 4.67 Ni−N components and split first-shell fits with 0.67 Ni−C and 4 Ni−N components were attempted. In the 4.67 Ni−N first-shell case, the fit improved slightly (F = 0.26), with very small changes in the σ^2 values of the remaining paths. Since the error in EXAFS coordination number determination is 25%, the fit cannot be differentiated from the best fit presented in Table 2. In the 0.67 Ni−C and 4 Ni−N first-shell case, again, the fit improved slightly (F = 0.26); however, the two first-shell paths (2.02 and 2.08 Å) were within the resolution of the data (∼0.10 Å), and the first-shell split was not justifiable. However, both fits are consistent with the best fit presented in Table 2 and support an axial Ni−C(methyl) interaction. It is important to note here that the Ni−C(methyl) interaction cannot be separated from the spread of Ni−N interactions. In addition, the σ^2 value of the Ni−N component is on the higher side (∼591), indicating that there is a spread in the first-shell bond distances, likely due to the presence of a shorter Ni−C(methyl) component. On the basis of the resolution of the data, the lower limit of the Ni−C bond distance is estimated to be 1.99 Å. The Ni−O bond distance from the weak glutamine ligand is ill-determined from the EXAFS fits. Since the Ni−C bond distance can be modulated by the transaxial ligand, DFT calculations were also performed in the absence of the transaxial ligand. The optimized Ni−C bond distance with and without the lower axial Ni−O ligand is 2.0 and 2.04 Å, respectively, which are both consistent with the EXAFS data and Ni−C bonds in model complexes, which range from 1.95 to 2.04 Å (*74*). In addition, a more than 3-fold increase in the pre-edge intensity of MCR_{Me} relative to $MCR_{red1-silent}$ suggests that the Ni−C bond is shorter than the average Ni−N distance. Thus, a combination of the Ni K-pre-edge intensity and energy position, DFT calculations, and the EXAFS data reveal a six-coordinate active site with a significantly weak axial Ni−O bond and an axial Ni−C bond with a bond distance of ∼2.04 Å (average of EXAFS and DFT bond distances) in MCR_{Me} (Figure 6).

DISCUSSION

Methyl-coenzyme M reductase catalyzes the reduction of methyl-coenzyme M (methyl-SCoM) with coenzyme B (HSCoB) to methane with the subsequent formation of the heterodisulfide of methyl-SCoM and HSCoB. Several experimental and theoretical studies have been performed in an effort to understand the catalytic mechanism of MCR and the geometric and electronic structures of the intermediates

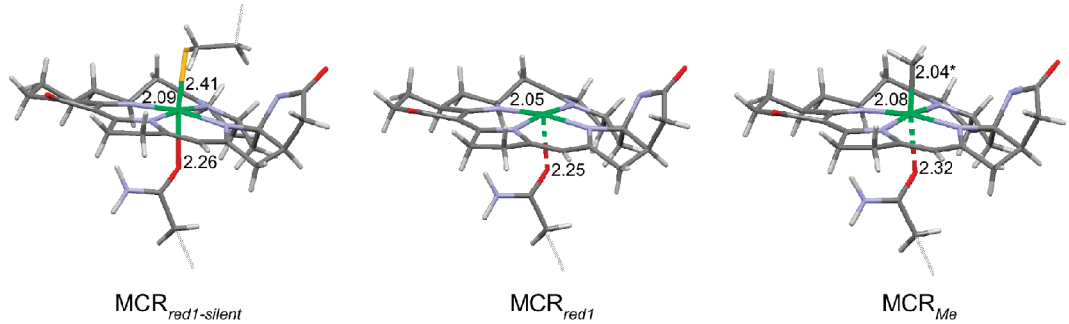

FIGURE 6: Schematic diagram of the predicted active site structures of $MCR_{red1-silent}$, MCR_{red1}, and MCR_{Me} based on Ni K-edge EXAFS and Ni K-pre-edge analysis. Relevant first-shell bond distances have been included. Some atoms of the F_{430} cofactor have been omitted for the sake of clarity. The lower-axial bond distance in MCR_{Me} is ill-determined by EXAFS. The dashed Ni−O bond in MCR_{red1} and MCR_{Me} indicates a larger than normal EXAFS uncertainty. Asterisks indicate the average Ni−C bond distance, based on TD-DFT calculations and EXAFS data analysis.

in the catalytic cycle, and to date, two mechanisms have been proposed, which differ in the first step: the reaction of MCR_{red1} with methyl-SCoM. The first mechanism involves the formation of an organometallic Ni^{III}−methyl intermediate starting from MCR_{red1} and methyl-SCoM. This is followed by protonolysis to generate methane and the heterodisulfide. The second mechanism involves a direct attack of the Ni^{I} on the S of methyl-SCoM, resulting in a homolytic cleavage of the thioether bond and formation of a Ni^{II}−thiolate species and a $CH_3^{\bullet}$ radical. The methyl radical reacts with HSCoB to form methane followed by subsequent heterodisulfide formation and reduction of the Ni^{II} species to MCR_{red1}. In the study presented here, the geometric and electronic structures of MCR_{red1} and of a stable Ni^{III}−methyl species (formed from the reaction of MCR_{red1} and MeI) have been elucidated using X-ray absorption spectroscopy.

The formation and stability of this species support the intermediacy of an alkyl−Ni species in the catalytic cycle of MCR, as proposed in mechanism I. The next step in the catalytic cycle (mechanism I) involves the cleavage of the Ni^{III}−methyl bond. This can occur either by homolytic cleavage resulting in Ni^{II} and a $CH_3^{\bullet}$ radical or by heterolytic cleavage involving two-electron transfer from the methyl group to the Ni center resulting in Ni^{I} and a CH_3^{+} cation. The results presented in this study indicate that the Ni−C bond in MCR_{Me} is long (*74*), reminiscent of the long Co^{III}−C bond in adenosylcobalamin (AdoCbl) (∼2.04 Å) (*75*) and in methylcobalamin (1.96−2.08 Å) (*76*). In AdoCbl-dependent enzymes, the long weak Co−C bond undergoes a homolytic cleavage forming an $Ado^{\bullet}$ radical, which subsequently initiates radical-based substrate rearrangements (*77*−*80*), while in MeCbl, a heterolytic cleavage occurs to leave a methyl cation and Co^{I}. Thus, the long Ni−Me bond in MCR observed by XAS could promote homolysis of the Ni^{III}−methyl bond, which would lead to formation of a methyl radical or enhance the electrophilicity of the methyl group, hence increasing its susceptibility toward nucleophilic attack. In the case of the radical mechanism, the resulting $CH_3^{\bullet}$ radical can then abstract an $H^{\bullet}$ from HSCoB (either directly or indirectly through another radical intermediate), yielding CH_4 and $^{\bullet}$SCoB, which subsequently would lead to the formation of CoBS-SCoM and the active MCR_{red1} state of MCR.

In this study, Ni K-pre-edge, rising-edge, and EXAFS data analysis have been combined with TD-DFT calculations on the $MCR_{red1-silent}$, MCR_{red1}, and MCR_{Me} states of MCR to elucidate the geometric and electronic structure differences. It is shown that the Ni K-pre-edge energies (1s → 3d transition) in all three states of MCR are higher than in most Ni complexes (≤8331.5 eV), which provides direct evidence for the strong Ni−F_{430} cofactor interaction in MCR. For $MCR_{red1-silent}$, high-*k* EXAFS data have been used to show that the geometric structure in solution is very similar to that obtained from the crystal structure, a six-coordinate active site with four Ni−N distances of 2.09 Å, one Ni−S distance of 2.41 Å, and one Ni−O distance of 2.26 Å. The data provide high-resolution first-shell bond distances (±0.02 error in bond distance estimation) that have not yet been achieved by X-ray diffraction measurements. For the MCR_{red1} state, a better understanding of the five-coordinate, reduced Ni^{I} active site has been achieved, and it is shown that the first-shell coordination is distorted with a large distribution of the Ni−N distances. The average Ni−N distance is 2.05 Å, and the shorter axial Ni−O distance is 2.25 Å. The first solution structure of an Ni^{III}−alkyl state of MCR, MCR_{Me}, has been determined, which shows that the active site is six-coordinate with four Ni−N distances of 2.08 Å, one Ni−C bond (∼2.04 Å), and a poorly determined lower axial Ni−O interaction of 2.32 Å.

The EXAFS analysis (combined with the Ni K-edge pre-edge data and DFT calculations) presented here unambiguously demonstrates the presence of a long Ni−C organometallic bond (*74*), which is attributed to an upper axial Ni^{III}−methyl interaction. The EXAFS data reveal that a weak axial Ni−O interaction is present in all three states of MCR, demonstrating that this axial ligand does not participate in strong bonding with the central Ni atom. It is therefore likely that the lower axial glutamine ligand is present to tune the redox potential and/or to provide stability to the active site.

The XAS data for the different forms of MCR show a unique property: the shift in the edge energy positions is relatively small, indicating that the Q_{Ni} on the Ni is similar in all the three states of MCR, consistent with the Ni K-edge EXAFS data. This demonstrates that the Ni−N bond distances have not changed significantly with the transition from MCR_{red1} to $MCR_{red1-silent}$ to MCR_{Me}. The similarity in charge for the three MCR states is a direct consequence of Pauling's electroneutrality principle which is manifested in this system by two different mechanisms. Upon reduction of $MCR_{red1-silent}$ to MCR_{red1}, the filled 3d orbitals on the Ni center are destabilized, allowing for back-bonding interaction between the Ni center and the F_{430} cofactor with a partial

flow of charge from the Ni to the F_{430} orbitals, and hence, the charge on the central Ni atom remains closer to that in $MCR_{red1-silent}$ (closer to Ni^{II} than Ni^{I}). This is consistent with the similar Löewdin charges on the Ni center in MCR_{red1} and $MCR_{red1-silent}$ obtained from DFT calculations (Table 3). Calculations also show a dramatic increase in the Ni $3d_{yz}$ and $3d_{xz}$ hole character due to back-bonding interaction with the filled π^* orbitals on the F_{430} ring. This increases the total valence Ni character, leading to similar charges on the Ni center in MCR_{red1} and $MCR_{red1-silent}$. With the transition from $MCR_{red1-silent}$ to MCR_{Me}, the additional 3d hole created in MCR_{Me} (Ni^{III} in d^7 configuration) undergoes covalent delocalization over the entire active site, resulting in a species that is best described as $[Ni(F_{430})Me]^+$. Thus, in this case also, the charge on the central Ni atom remains closer to that in $MCR_{red1-silent}$. Since the total charge on the $MCR_{red1-silent}$ and MCR_{Me} models chosen for the DFT calculations are different, a direct comparison of the individual fragment charges will be inaccurate; however, the combined valence Ni 3d character in MCR_{red1} (150%) and $MCR_{red1-silent}$ (141%) are similar, with only a small increase for MCR_{Me}. This, combined with the small edge shift with the transition from $MCR_{red1-silent}$ to MCR_{Me}, indicates similar charges in the two states. This noninnocent role of the F_{430} cofactor in tuning its bonding with the Ni center in different oxidation states is expected to play a direct role in modulating the geometric and electronic structures of the active site and therefore plays an important role in the catalytic pathway. For example, it might be expected that the Ni^{III} site in MCR_{Me} would be very unstable due to a high redox potential and might spontaneously reduce to form a Ni^{II}−methyl species. The stability of the MCR_{Me} can be attributed to the noninnocent participation of the F_{430} cofactor in bonding, which is consistent with the stability observed in reported biochemical studies performed with this state of MCR. In the case of MCR_{red1}, the low charge on a formally Ni^{I} species would be expected to increase the pK_a of the coordinating anionic nitrogen on the F_{430} ring and destabilize the Ni−N bond toward dissociation and protonation. Here again, the participation of the F_{430} ring in noninnocent bonding results in an increase in Q_{Ni} and promotes the stability of the MCR_{red1} species. Thus, the Ni K-edge XAS data indicate that the F_{430} cofactor plays a critical role in stabilizing the different forms of MCR and tuning the reactivity of the protein.

ACKNOWLEDGMENT

SSRL operations are funded by the Department of Energy, Office of Basic Energy Sciences. The SSRL Structural Molecular Biology program is supported by the National Institutes of Health, National Center for Research Resources, Biomedical Technology Program, and the Department of Energy, Office of Biological and Environmental Research.

SUPPORTING INFORMATION AVAILABLE

Figures and table showing the FEFF fits to the Ni K-edge EXAFS data and their corresponding Fourier transforms of the $MCR_{red1-silent}$ subtracted MCR_{red1} and MCR_{Me} forms and the metrical parameters, respectively, and a shell-by-shell analysis of the EXAFS data for MCR_{red1}, $MCR_{red1-silent}$, and MCR_{Me}. This material is available free of charge via the Internet at http://pubs.acs.org.

REFERENCES

1. Thauer, R. K. (1998) Biochemistry of methanogenesis: A tribute to Marjory Stephenson. *Microbiology 144*, 2377–2406.
2. DiMarco, A. A., Bobik, T. A., and Wolfe, R. S. (1990) Unusual coenzymes of methanogenesis. *Annu. Rev. Biochem. 59*, 355–394.
3. Ellermann, J., Hedderich, R., Böcher, R., and Thauer, R. K. (1988) The final step in methane formation: Investigations with highly purified methyl-coenzyme M reductase (component C) from *Methanobacterium thermoautotrophicum* (strain Marburg). *Eur. J. Biochem. 172*, 669–678.
4. Ellefson, W. L., Wolfe, R. S., and Whitman, W. B. (1982) Nickel-containing factor F430: Chromophore of the methyl reductase of *Methanobacterium thermoautotrophicum*. *Proc. Natl. Acad. Sci. U.S.A. 79*, 3707–3710.
5. Färber, G., Keller, W., Kratky, C., Jaun, B., Pfaltz, A., Spinner, C., Kobelt, A., and Eschenmoser, A. (1991) Coenzyme F430 from methanogenic bacteria: Complete assignment of configuration based on X-ray analysis of 12,13-Diepi-F430 pentamethyl ester and on NMR spectroscopy. *Helv. Chim. Acta 74*, 697–716.
6. Shima, S., and Thauer, R. K. (2005) Methyl-coenzyme M reductase and the anaerobic oxidation of methane in methanotrophic archaea. *Curr. Opin. Microbiol. 8*, 643–648.
7. Thauer, R. K., and Shima, S. (2008) Methane as fuel for anaerobic microorganisms. *Ann. N.Y. Acad. Sci. 1125*, 158–170.
8. Duin, E. C., Cosper, N. J., Mahlert, F., Thauer, R. K., and Scott, R. A. (2003) Coordination and geometry of the nickel atom in active methyl-coenzyme M reductase from *Methanothermobacter marburgensis* as detected by X-ray absorption spectroscopy. *J. Biol. Inorg. Chem. 8*, 141–148.
9. Signor, L., Knuppe, C., Hug, R., Schweizer, B., Pfaltz, A., and Jaun, B. (2000) Methane formation by reaction of a methyl thioether with a photo-excited nickel thiolate: A process mimicking methanogenesis in archaea. *Chem.—Eur. J. 6*, 3508–3516.
10. Grabarse, W., Mahlert, F., Duin, E. C., Goubeaud, M., Shima, S., Thauer, R. K., Lamzin, V., and Ermler, U. (2001) On the mechanism of biological methane formation: Structural evidence for conformational changes in methyl-coenzyme M reductase upon substrate binding. *J. Mol. Biol. 309*, 315–330.
11. Duin, E. C., and McKee, M. L. (2008) A new mechanism for methane production from methyl-coenzyme M reductase as derived from density functional calculations. *J. Phys. Chem. B 112*, 2466–2482.
12. Pelmenschikov, V., and Siegbahn, P. E. (2003) Catalysis by methyl-coenzyme M reductase: A theoretical study for heterodisulfide product formation. *J. Biol. Inorg. Chem. 8*, 653–662.
13. Pelmenschikov, V., Blomberg, M. R., Siegbahn, P. E., and Crabtree, R. H. (2002) A mechanism from quantum chemical studies for methane formation in methanogenesis. *J. Am. Chem. Soc. 124*, 4039–4049.
14. Grabarse, W. G., Mahlert, F., Shima, S., Thauer, R. K., and Ermler, U. (2000) Comparison of three methyl-coenzyme M reductases from phylogenetically distant organisms: Unusual amino acid modification, conservation and adaptation. *J. Mol. Biol. 303*, 329–344.
15. Tang, Q., Carrington, P. E., Horng, Y. C., Maroney, M. J., Ragsdale, S. W., and Bocian, D. F. (2002) X-ray absorption and resonance Raman studies of methyl-coenzyme M reductase indicating that ligand exchange and macrocycle reduction accompany reductive activation. *J. Am. Chem. Soc. 124*, 13242–13256.
16. Yang, N., Reiher, M., Wang, M., Harmer, J., and Duin, E. (2007) Formation of a nickel-methyl species in methyl-coenzyme M reductase, an enzyme catalyzing methane formation. *J. Am. Chem. Soc. 129*, 11028–11029.
17. Dey, M., Telser, J., Kunz, R. C., Lees, N. S., Ragsdale, S. W., and Hoffman, B. M. (2007) Biochemical and spectroscopic studies of the electronic structure and reactivity of a methyl-Ni species formed on methyl-coenzyme M reductase. *J. Am. Chem. Soc. 129*, 11030–11032.
18. Kunz, R. C., Horng, Y. C., and Ragsdale, S. W. (2006) Spectroscopic and kinetic studies of the reaction of bromopropanesulfonate with methyl-coenzyme M reductase. *J. Biol. Chem. 281*, 34663–34676.
19. Kunz, R. C., Dey, M., and Ragsdale, S. W. (2008) Characterization of the thioether product formed from the thiolytic cleavage of the

alkyl-nickel bond in methyl-coenzyme M reductase. *Biochemistry 47*, 2661–2667.
20. Dey, M., Kunz, R. C., Lyons, D. M., and Ragsdale, S. W. (2007) Characterization of alkyl-nickel adducts generated by reaction of methyl-coenzyme M reductase with brominated acids. *Biochemistry 46*, 11969–11978.
21. Hinderberger, D., Piskorski, R. P., Goenrich, M., Thauer, R. K., Schweiger, A., Harmer, J., and Jaun, B. (2006) A nickel-alkyl bond in an inactivated state of the enzyme catalyzing methane formation. *Angew. Chem., Int. Ed. 45*, 3602–3607.
22. Tenderholt, A. *Pyspline* and *QMForge*.
23. George, G. *EXAFSPAK* and *EDG-FIT*.
24. Rehr, J., and Albers, R. (2000) Theoretical approaches to X-ray absorption fine structure. *Rev. Mod. Phys. 72*, 621–654.
25. Mustre de Leon, J., Rehr, J., Zabinsky, S., and Albers, R. (1991) Ab initio curved wave X-ray absoprtion fine structure. *Phys. Rev. B: Condens. Matter Mater. Phys. 44*, 4146–4156.
26. Rehr, J., Mustre de Leon, J., Zabinsky, S., and Albers, R. (1991) Theoretical X-ray absorption fine structure standards. *J. Am. Chem. Soc. 113*, 5135–5140.
27. Ermler, U., Grabarse, W., Shima, S., Goubeaud, M., and Thauer, R. K. (1997) Crystal structure of methyl-coenzyme M reductase: The key enzyme of biological methane formation. *Science 278*, 1457–1462.
28. Stern, E. A. (1993) Number of relevant independent points in X-ray absorption fine structure spectra. *Phys. Rev. B: Condens. Matter Mater. Phys. 48*, 9825–9827.
29. Pople, J. (2004)*Gaussian 03*, revision C.02.
30. Lee, C., Yang, W., and Parr, R. (1988) Development of the Colle-Salvetti correlation-energy formula into a functional of the electron density. *Phys. Rev. B: Condens. Matter Mater. Phys. 37*, 785–789.
31. Mihelich, B., Savin, A., Stoll, H., and Preuss, H. (1989) Results obtained with the correlation energy density functionals of Becke and Lee, Yang and Parr. *Chem. Phys. Lett. 157*, 200–206.
32. Becke, A. (1993) Density functional theromochemistry: 3. The role of exact exchange. *J. Chem. Phys. 98*, 5648–5652.
33. Krishnan, R., Binkley, J., Seeger, R., and Pople, J. (1980) Self consistent molecular-orbital methods. 20. Basis set for correlated wave functions. *J. Chem. Phys. 72*, 650–654.
34. McGrath, M., and Radom, L. (1991) Extension of Gaussian-1 (G1) theory to bromine-containing molecules. *J. Chem. Phys. 94*, 511–516.
35. Curtiss, L., McGrath, M., Blaudeau, J., Davis, N., BInning, R., and Radom, L. (1995) Extension of Gaussian-2 theory to molecules containing 3rd row atoms Ga-Kr. *J. Chem. Phys. 103*, 6104–6113.
36. Rassolov, V. A., Pople, J. A., Ratner, M. A., and Windus, T. L. (1998) 6-31G* basis set for atoms K through Zn. *J. Chem. Phys. 109*, 1223–1229.
37. Hariharan, P., and Pople, J. (1973) The influence of polarization functions on molecular orbital hydrogenation energies. *Theor. Chim. Acta 28*, 213–222.
38. Francl, M., Pietro, W., Hehre, W., Binkley, J., Gordon, M., DeFrees, D., and Pople, J. (1982) Self consistent molecular-orbital methods. 23. A polarization type basis set for 2nd-row elements. *J. Chem. Phys. 77*, 3654–3665.
39. Neese, F. (2004)*ORCA: An ab initio, DFT and semiempirical Electronic Structure Package*.
40. Neese, F., and Olbrich, G. (2002) Efficient use of the resolution of the identity approximation in time-dependent density functional calculations with hybrid density functionals. *Chem. Phys. Lett. 362*, 170–178.
41. Neese, F. (2002) Prediction and interpretation of the Fe-57 isomer shift in M. *Chim. Acta 337*, 181–192.
42. Sinnecker, S., Slep, L., Bill, E., and Neese, F. (2005) Performance of nonrelativistic and quasi-relativistic hybrid DFT for the prediction of electric and magnetic hyperfine parameters in Fe-57 M spectra. *Inorg. Chem. 44*, 2245–2254.
43. Schaefer, A., Horn, H., and Ahlrichs, R. (1992) Fully optimized contracted Gaussian basis sets for atoms Li to Kr. *J. Chem. Phys. 97*, 2571–2577.
44. Schaefer, A., Huber, C., and Ahlrichs, R. (1994) Fully optimized contracted Gaussian basis sets of triple-ζ valence quality for atoms Li to Kr. *J. Chem. Phys. 100*, 5829–5835.
45. Krause, M., and Oliver, J. (1979) Natural widths of the atomic K-levels and L-levels, K-alpha X-ray lines and several KLL Auger lines. *J. Phys. Chem. Ref. Data 8*, 329–338.
46. UV−vis absorption measurements on the MCR_{red1} and MCR_{Me} samples showed 36 and 33% $MCR_{red1-silent}$ contamination, respectively. The $MCR_{red1-silent}$ spectrum has been quantitatively subtracted from the MCR_{red1} and MCR_{Me} spectra, and the data have been renormalized.
47. Shulman, R. G., Yafet, Y., Eisenberger, P., and Blumberg, W. E. (1976) Observation and interpretation of X-ray absorption edges in iron compounds and proteins. *Proc. Natl. Acad. Sci. U.S.A. 73*, 1384–1388.
48. Penner-Hahn, J. E., Scott, R. A., Hodgson, K. O., Doniach, S., Desjardins, S. R., and Solomon, E. I. (1982) Observation of an electric quadrupole transition in the X-ray absorption spectrum of a Cu(II) complex. *Chem. Phys. Lett. 88*, 595–598.
49. Westre, T. E., Kennepohl, P., DeWitt, J. G., Hedman, B., Hodgson, K. O., and Solomon, E. I. (1997) A multiplet analysis of Fe K-edge 1s → 3d pre-edge features of iron complexes. *J. Am. Chem. Soc. 119*, 6297–6314.
50. Sarangi, R., Aboelella, N., Fujisawa, K., Tolman, W. B., Hedman, B., Hodgson, K. O., and Solomon, E. I. (2006) X-ray absorption edge spectroscopy and computational studies on LCu O_2 species: Superoxide-CuII versus peroxide-CuIII bonding. *J. Am. Chem. Soc. 128*, 8286–8296.
51. Sarangi, R., Frank, P., Hodgson, K. O., and Hedman, B. (2008) When identical functional groups are not identical: A DFT study of the effects of molecular environment on sulfur K-edge X-ray absorption spectra. *Inorg. Chim. Acta 361*, 956–964.
52. Teo, B. (1986) *EXAFS: Basic Principles and Data Analysis*, Springer-Verlag, Berlin.
53. R' denotes the non-phase shift corrected bond distance.
54. The traditional E_0 value for the Ni K-edge is 8340 eV. However, as seen in Figure 2, 8340 eV is well below the white line and is too low to be the threshold energy in the data presented here. This is adjusted in the fits with a ΔE_0 value of ∼13 eV, which changes the E_0 value in the fits to ∼8353 eV. This value is above the white line and hence is a theoretically justifiable choice.
55. Cheesman, M. R., Ankel-Fuchs, D., Thauer, R. K., and Thompson, A. J. (1989) The magnetic properties of the nickel cofactor F430 in the enzyme methyl-coenzyme M reductase of *Methanobacterium thermoautotrophicum*. *Biochem. J. 260*, 613–616.
56. Hamilton, C. L., Scott, R. A., and Johnson, M. K. (1989) The magnetic and electronic properties of *Methanobacterium thermoautotrophicum* (strain delta H) methyl coenzyme M reductase and its nickel tetrapyrrole cofactor F430. A low temperature magnetic circular dichroism study. *J. Biol. Chem. 264*, 11605–11613.
57. Telser, J., Davydov, R., Horng, Y. C., Ragsdale, S. W., and Hoffman, B. M. (2001) Cryoreduction of methyl-coenzyme M reductase: EPR characterization of forms, MCR_{ox1} and MCR_{red1}. *J. Am. Chem. Soc. 123*, 5853–5860.
58. Craft, J. L., Horng, Y.-C., Ragsdale, S. W., and Brunold, T. C. (2004) Nickel oxidation states of F430 cofactor in methyl-coenzyme M reductase. *J. Am. Chem. Soc. 126*, 4068–4069.
59. Colpas, G. J., Maroney, M. J., Bagyinka, C., Kumar, M., Willis, W. S., Suib, S. L., Baidya, N., and Mascharak, P. K. (1991) X-ray spectroscopies studies of nickel complexes, with application to the structure of nickle sites in hydrogenases. *Inorg. Chem. 30*, 920–928.
60. Szilagyi, R. K., Lim, B. S., Glaser, T., Holm, R. H., Hedman, B., Hodgson, K. O., and Solomon, E. I. (2003) Description of the ground state wave functions of Ni dithiolenes using sulfur K-edge X-ray absorption spectroscopy. *J. Am. Chem. Soc. 125*, 9158–9169.
61. Furenlid, L. R., Renner, M. W., Smith, K. M., and Fajer, J. (1990) Structural consequences of nickel versus macrocycle reductions in F430 models: EXAFS studies of a Ni(I) anion and Ni(II) $\cdot\pi\cdot$anion radicals. *J. Am. Chem. Soc. 112*, 1634–1635.
62. Dey, M., Kunz, R. C., Van Heuvelen, K. M., Craft, J. L., Horng, Y. C., Tang, Q., Bocian, D. F., George, S. J., Brunold, T. C., and Ragsdale, S. W. (2006) Spectroscopic and computational studies of reduction of the metal versus the tetrapyrrole ring of coenzyme F430 from methyl-coenzyme M reductase. *Biochemistry 45*, 11915–11933.
63. Frank, P., Benfatto, M., Hedman, B., and Hodgson, K. O. (2008) Solution $[Cu(amm)]^{2+}$ is a strongly solvated square pyramid: A full account of the copper K-edge XAS spectrum within single-electron theory. *Inorg. Chem. 47*, 4126–4139.
64. Bair, R. A., and Goddard, W. A. I. (1980) Ab initio studies of the X-ray absorption edge in copper complexes. I. Atomic Cu^{2+} and $Cu(II)Cl_2$. *Phys. Rev. B: Condens. Matter Mater. Phys. 22*, 2767–2776.
65. Kosugi, N., Yokoyama, T., Asakura, K., and Kuroda, H. (1984) Polarized Cu K-edge XANES of square planar $CuCl_4^{2+}$ ion.

Experimental and theoretical evidence for shake-down phenomena. *Chem. Phys. 91*, 249–256.
66. Sarangi, R., DeBeer George, S., Rudd, D. J., Szilagyi, R. K., Ribas, X., Rovira, C., Almeida, M., Hodgson, K. O., Hedman, B., and Solomon, E. I. (2007) Sulfur K-edge X-ray absorption spectroscopy as a probe of ligand-metal bond covalency: Metal vs ligand oxidation in copper and nickel dithiolene complexes. *J. Am. Chem. Soc. 129*, 2316–2326.
67. Craft, J. L., Horng, Y.-C., Ragsdale, S. W., and Brunold, T. C. (2004) Spectroscopic and computational characterization of the nickel-containing F430 cofactor of methyl-coenzyme M reductase. *J. Biol. Inorg. Chem. 9*, 77–89.
68. The reported average standard deviation in bond distances in 1HBO (Cruickshank's DPI) is approximately ±0.14 Å (although the standard deviation in the Ni−N bond distances is expected to be better), while that for the Ni−N bond distances obtained from the EXAFS data is ±0.02 Å.
69. Although the resolution of $k = 2-17$ Å EXAFS data is ∼0.1 Å, the standard deviation of the first shell obtained from the EXAFS data presented here is ±0.02 Å.
70. Furenlid, L. R., Renner, M. W., and Fajer, J. (1990) EXAFS studies of nickel(II) and nickel(I) factor 430M. Conformational flexibility of the F430 skeleton. *J. Am. Chem. Soc. 112*, 8987–8989.
71. Shiemke, A. K., Shelnutt, J. A., and Scott, R. A. (1989) Coordination chemistry of F430: Axial ligation equilibrium between square-planar and bis-aquo species in aqueous solution. *J. Biol. Chem. 264*, 11236–11245.
72. Dey, M., Kunz, R. C., Van Heuvelen, K. M., Craft, J. L., Horng, Y.-C., Tang, Q., Bocian, D. F., George, S. J., Brunold, T. C., and Ragsdale, S. W. (2006) Spectroscopic and computational studies of reduction of the metal versus the tetrapyrrole ring of coenzyme F430 from methyl-coenzyme M reductase. *Biochemistry 45*, 11915–11933.
73. Duin, E. C., Signor, L., Piskorski, R., Mahlert, F., Clay, M. D., Goenrich, M., Thauer, R. K., Jaun, B., and Johnson, M. K. (2004) Spectroscopic investigation of the nickel-containing porphinoid cofactor F430. Comparison of the free cofactor in the (+)1, (+)2 and (+)3 oxidation states with the cofactor bound to methyl-coenzyme M reductase in the silent, red and ox forms. *J. Biol. Inorg. Chem. 9*, 563–576.
74. On the basis of ∼160 structures submitted to the Cambridge Structure Database (CSD), the average Ni−C(alkyl) bond distance in Ni^{I}- and Ni^{II}-containing complexes is ∼1.98 Å.
75. Ouyang, L., Rulis, P., Ching, W. Y., Nardin, G., and Randaccio, L. (2004) Accurate redetermination of the X-ray structure and electronic bonding in adenosylcobalamin. *Inorg. Chem. 43*, 1235–1241.
76. Drennan, C. L., Huang, S., Drummond, J. T., Matthews, R. G., and Ludwig, M. L. (1994) How a protein binds B12: A 3.0 Å X-ray structure of B12-binding domains of methionine synthase. *Science 266*, 1669–1674.
77. Marsh, E. N., and Drennan, C. L. (2001) Adenosylcobalamin-dependent isomerases: New insights into structure and mechanism. *Curr. Opin. Chem. Biol. 5*, 499–505.
78. Banerjee, R. (2001) Radical peregrinations catalyzed by coenzyme B12-dependent enzymes. *Biochemistry 40*, 6191–6198.
79. Ludwig, M. L., and Matthews, R. G. (1997) Structure-based perspectives on B12-dependent enzymes. *Annu. Rev. Biochem. 66*, 269–313.
80. Warncke, K., Schmidt, J. C., and Ke, S. C. (1999) Identification of a rearranged-substrate, product radical intermediate and the contribution of a product radical trap in vitamin B-12 coenzyme-dependent ethanolamine deaminase catalysis. *J. Am. Chem. Soc. 121*, 10522–10528.

BI900087W